RESEARCH ARTICLE

A Bionic Starfish Adsorption Crawling Soft Robot

Xiangang Huang[1] · Chenghao Zhang[1] · Wenqi Feng[1] · Xiangye Zhang[1] · Deyuan Zhang[1] · Yanqiang Liu[1]

Abstract
A variety of soft wall-climbing robots have been developed that can move in certain patterns. Most of these soft robots can only move on conventional surfaces and lack adaptability to complex surfaces. Improving the adaptability of soft robots on complex surfaces is still a challenging problem. To this end, we study the layered structure of the starfish tube foot and the valve flap structure in the water vascular system, and use an ultrasonic stress detector to study the stiffness distribution of the arm structure. Inspired by the motion of the starfish, we present a bionic soft wall-climbing robot, which is driven by two groups of pneumatic feet and achieves body bending through active adaptation layers. We design the structure of the foot to flex to provide driving force, and there are suction cups at the end of the foot to provide suction. The soft foot has a simple structure design, adapts to a variety of surfaces, and does not damage the surface of the substrate. Variable stiffness layers achieve stiffness changes by the principle of line blocking. The Central Pattern Generator theory is introduced to coordinately control the multiple feet of the robot. After experiments, we verify the adaptability of the soft robot to curved surfaces. The research may provide a reference for the design and development of crawling soft robots on complex surfaces.

1 Introduction

The research on traditional robots is mainly based on rigid structures, which have been widely accumulated and applied in industrial, medical and other fields. However, traditional robots have complex structures, limited flexibility, poor safety and adaptability. Soft robots made of soft materials can arbitrarily change their shape and size within a certain range, theoretically have infinite degrees of freedom, and have good environmental adaptability.

At present, many researchers have developed a variety of soft robots [1–7]. According to the functions, soft robots can be mainly divided into soft grasping robots and soft mobile robots [8]. Shintake et al. made a gripper made of dielectric elastomer, which is driven by electrostatic force to generate mechanical clamping force [9]. Pi et al. proposed a three-finger flexible bionic robot gripper. The main body of the robot was made of silicone rubber, which could grasp

objects [10]. Manti et al. made a cable-actuated soft hand. It consisted of three identical soft fingers that were connected to a rigid frame and were activated by a DC motor through a cable-based underactuated mechanism [11]. Gong et al. made a pneumatically driven soft hand. It consisted of four parts: two bending segments, one stretching segment, and one soft gripper [12]. Wang et al. designed a new dual-arm soft robotic manipulator. It realized the cooperation and grasping of a dual-arm manipulator [13]. All the research work they do is excellent. However, these grabbing robots are generally fixed on some rigid supports to realize the grabbing function. They cannot actively drive the movement of the rigid support.

In terms of soft mobile robots, inspired by the muscle–skeleton architecture of the human arm, Liu et al. designed a somatosensitive film soft crawling robot (SFSCR) for load carrying and multi-terrain locomotion [14]. Bartlett et al. made a soft bouncing robot. This robot is able to perform untethered jumping [15]. Inspired by an arboreal snake's winding climbing locomotion, Liao et al. proposed a tethered winding-styled soft rod-climbing robot. It was capable of crawling on poles or tubes [16]. Chen et al. presented a cable-driven switching-legged inchworm-inspired soft robot that could perform basic movements in multiple conditions

✉ Yanqiang Liu
liuyanqiang@buaa.edu.cn

1 Institute of Bionic and Micro-Nano Systems, School of Mechanical Engineering and Automation, Beihang University, Beijing 100191, China

as different surface frictions and slopes [17]. Kandhari et al. designed a fabric-based worm-like robot with capable of peristaltic locomotion [18]. Zheng et al. designed miniature piezoelectric three-legged crawling robots that achieved the movements in six different directions [19]. Su et al. presented a novel pneumatic leech-like soft robot, Leechbot, with both bending and stretching deformation for locomotion. Leechbot could crawl on surfaces in different orientations [20].

Starfish is a typical echinoderm. Most species of starfish have five-spoke symmetry in their adult bodies, which have the functions of adsorption and movement. Many researchers have carried out bionic research on starfish and made many soft robots. Jin et al. studied a modular starfish-like robot driven by SMA wires. It was capable of omnidirectional motion [21]. Yang et al. introduced the micro-tube feet structures of starfish into their robot design. Their method could enhance the obstacle-climbing ability [22]. Munadi et al. developed a low-cost soft quadrupedal starfish soft robot which could walk in straightforward direction using undulating gait cycle [23]. Poungrat et al. designed a modular soft robot driven by a pneumatic artificial muscle and tested different locomotion gaits [24].

Although a variety of soft wall-climbing robots have been developed that can move in certain modes, their application scenarios are still very limited. Some soft robots can only move on regular surfaces. Some can only move on certain rods or pipes. Some do not provide sufficient adhesion. Few of them can move on complex surfaces. Therefore, improving the adaptability of soft robots on complex surfaces is a challenging problem.

To this end, we propose a new type of bionic starfish adsorption crawling soft robot. It can adapt to complex surfaces with multiple curvature changes, because it can bend in two directions, and the flexible tube feet similar to starfish can fit the surface perfectly. At the same time, like the starfish, this robot has the function of stiffness change, and the stiffness is small in the motion state, which is easy to adapt to the curved surface. Its rigidity becomes larger in the stop state, and various functions can be realized, such as detection and processing. The soft robot is very simple to make, made of only one type of silicone. A positive pressure air source, a negative pressure air source and multiple solenoid valve controls can realize complex movements.

To test the performance of the robot, we did a series of experiments, including the relationship between the elongation length of the tube foot and the air pressure, the relationship between the bending angle of the active adaptation layer and the air pressure, and the relationship between the variable stiffness structure force and displacement. The robot has achieved the desired effect and has good adaptability to curved surfaces. Soft robots have great application potential in inspection and maintenance. For example,

a camera-mounted starfish soft robot can perform flaw detection on the interior surface of an aircraft (Fig. 1).

2 Biological Study of Starfish

2.1 Hierarchical Structure of Starfish Tube Feet

The extension and shortening of the tube foot are powered by the contraction and relaxation of the ampulla muscle. When the tube foot is extended, the ampulla muscle will contract and the ampulla volume will decrease. At this time, the liquid in the ampulla will enter the tube foot under pressure, causing the tube foot to stretch. When the tube foot is shortened, the ampulla relaxes, and the liquid in the ampulla flows from the tube foot into the ampulla, which shortens the tube foot.

The section cut along the longitudinal direction of the starfish tube foot is shown in Fig. 2. The figure shows that the structure is composed of connective tissue fibers arranged in a cross-fiber spiral array. This array of connective tissue fibers is wrapped in a left–right symmetrical spiral structure.

The angle formed by the connective tissue fibers and the long axis of the starfish tube foot is defined as the fiber angle, which is about 67° and is relatively constant along the long axis of the starfish tube foot.

2.2 The Valve Flap Structure of Starfish

The valve flap is a structure located at the junction of the radial canal and the tube foot. It is the tubular extension part of the radial canal entering the tube foot cavity and extending into its orifice. The valve flap can be closed to the middle through muscle contraction, so as to reduce or close the lateral neck.

Figure 2b shows the position of the starfish valve flap. It does not bend parallel to the direction of the tube foot when sliced, and the tube foot can be approximately regarded as a
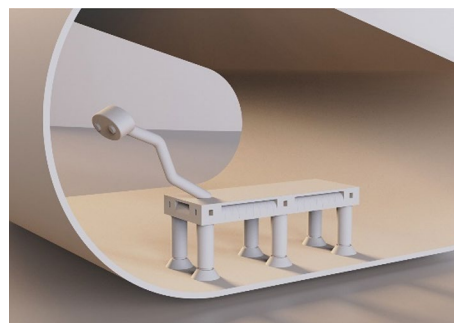

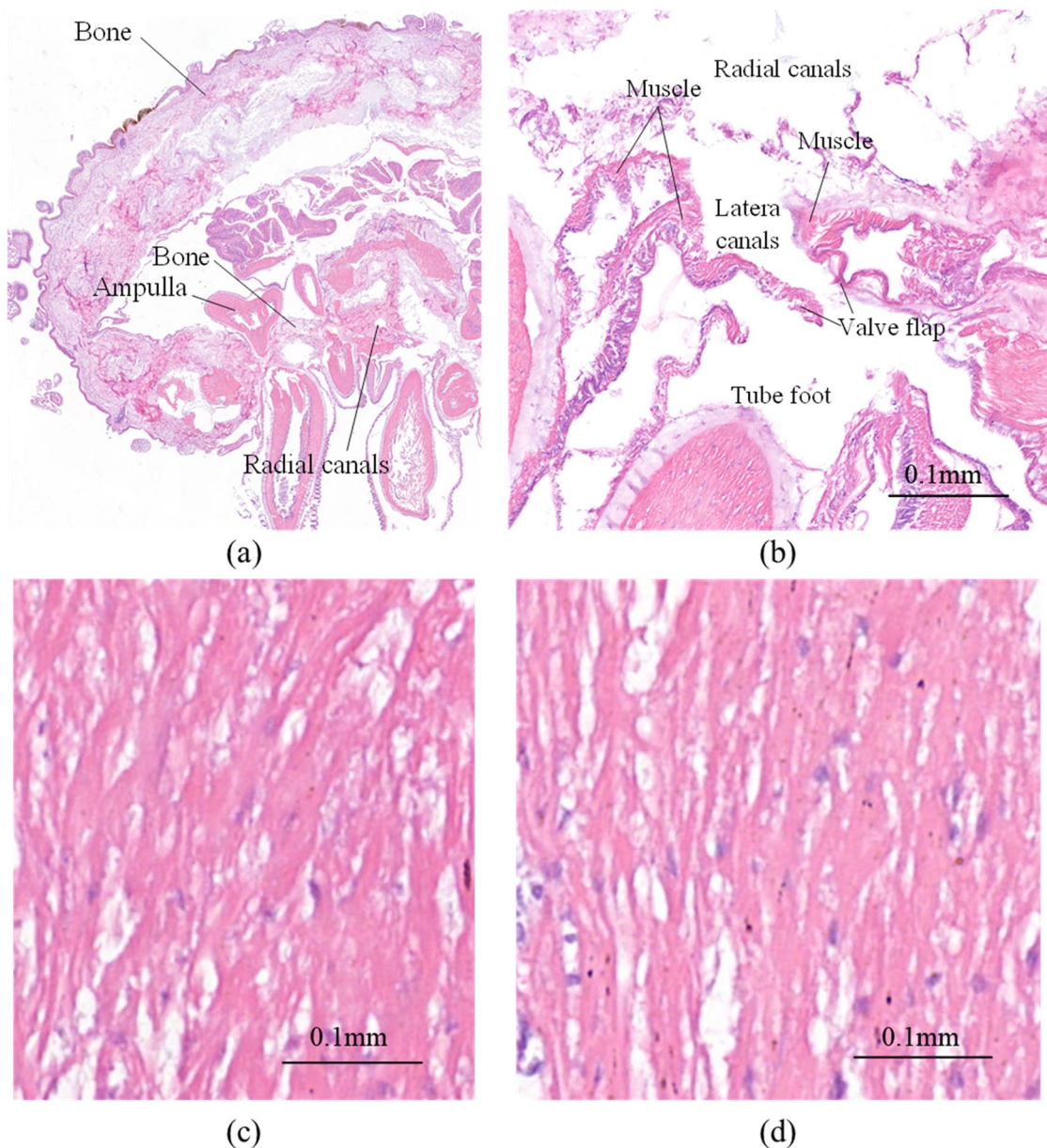**Fig. 1** The future working environment of soft robots

Fig. 2 Biological structure of starfish. **a** Tube foot and ampulla; **b** the position of starfish valve flap; **c** cross-fiber section 1; **d** cross-fiber section 2

cylinder, so the cross-section of the tube foot is circular arc, with a scale of 0.1 mm.

The structure of the valve flap determines that the liquid can only flow from the radial canal to the tube foot instead of in the reverse direction, which is one-way flow. Muscle fibers grow from the top and side walls of the side of the radial canal, and then connect to the valve flap. Therefore, the presence of muscle fibers allows the valve flap to open and close actively. The valve flap is composed of a thin layer of connective tissue. A simple squamous epithelium covers the thin layer of connective tissue and continues to connect with the epithelium of the tube foot and the radial canal.

According to the measured results of cross-section materials, some studies have shown that the volume of fluid in the radial canal and lateral neck of medium starfish does not exceed 1–2% of the total capacity of all ampulla systems. Therefore, the ampulla cannot replenish sufficient fluid from this unbalanced supply system to facilitate large-scale motion. Therefore, the ampulla and feet of a starfish form a relatively closed system, while a small amount of fluid lost in motion due to penetration caused by high pressure inside the ampulla is supplemented by the radial canal structure.
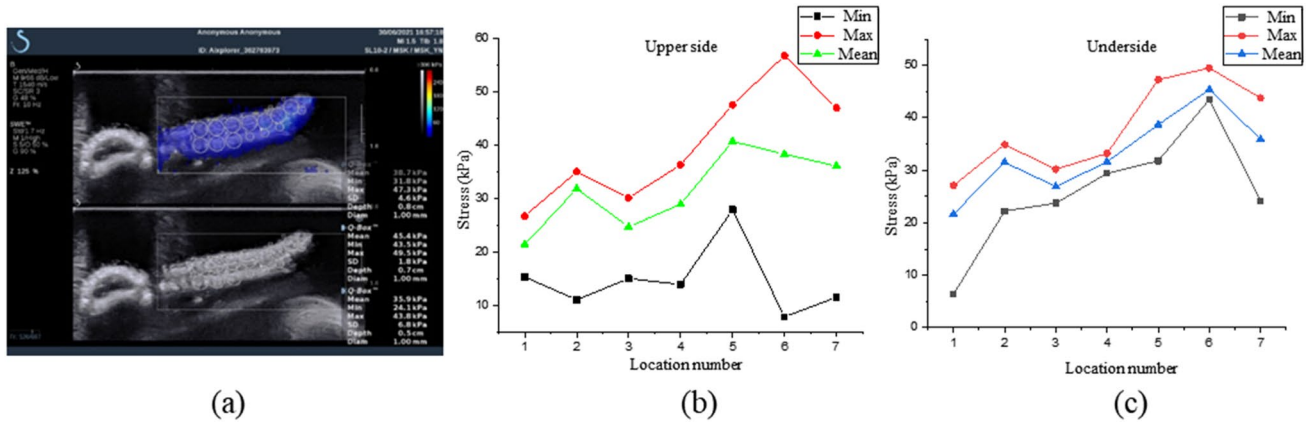
Fig. 3 Stiffness distribution diagram of starfish arm stretching and suspended. **a** Experimental picture; **b** the stiffness distribution of the upper part of the starfish arm; **c** the stiffness distribution of the lower part of the starfish arm

2.3 Study on the Stiffness of Starfish Arm Structure

Most of the studies on living starfish focus on behavioral physiology. There are relatively few studies on the internal structure of living starfish. Therefore, to explore the dynamic changes of the internal structure of living starfish, it is an important aspect to study the stiffness changes of starfish arm structure in various states.

Ultrasound stress detection technology has many advantages such as good penetration and strong orientation. It is widely used in metal material detection in mechanical field, concrete stress detection in civil engineering field, viscera detection in medical field, etc. To study the dynamic changes of the internal structure of living starfish, an ultrasonic stress tester can be used to study the starfish. The ultrasonic stress tester can obtain the stress of each detected part and indirectly reflect the stiffness of each part.

To study the stiffness of starfish's arm, the equipment used is an ultrasonic stress detector, and the starfish is in a living state. At the beginning of the experiment, the starfish was put into the equipment. There were two states taken into consideration: whether the arm ends were suspended or not, in which the dynamic stiffness of the starfish's arm when stretching and bending was monitored and the video file was exported. In the video file, the stiffness of different areas of the starfish's arm in various states was recorded and a graph was drawn.

The side view of the starfish's arm in the extended state is shown in Fig. 3a, and the starfish's arm is in a suspended state at the same time. Each circle in the figure is a sampling area, corresponding to each point in the curve from left to right. The return value measured in each area

has maximum value (Max), minimum value (Min) and average value (Mean). The stress changes on the upper and lower sides of the arm are shown in the two graphs, respectively. The results show that the stiffness of the starfish arms generally increases from the root to the end.

The side view of the extended starfish arm is shown in Fig. 4a, with the end of the starfish arm supported and the middle section overhanging. Figure 4c shows a side view of the bent starfish arm with the end of the arm touching the bottom surface. At this point, the arm is supported at both ends and the middle section is bent and overhanging. Figure 4b and d shows the stress data in the two cases, respectively. From Fig. 4b, it can be seen that the stiffness of the end and root of the starfish arm is relatively large, and the stiffness of the middle overhanging part is relatively small. The overall trend of the stiffness values from the root to the end is first decreasing and then increasing. From Fig. 4d, it can be seen that the stiffness of the end and root of the starfish arm is smaller, and the stiffness of the middle bending and overhanging part is larger. From the root to the end, the stiffness value tends to rise first and then fall. The possible reason for this phenomenon is that the muscles located on the arm contract when the arm is bent, making the structure of the bent part denser. Therefore, the stiffness is greater when the arm is bent compared to when the arm is naturally extended.

We took a side view of the extended starfish arm (Fig. 5), and selected two long regions of the upper and lower parts of the starfish arm. The stiffness of the upper side of the starfish arm is smaller than that of the lower side, regardless of whether the starfish arm is in the suspended or landed state. The data are shown in Table 1. It can be seen that when the starfish is suspended in the air,
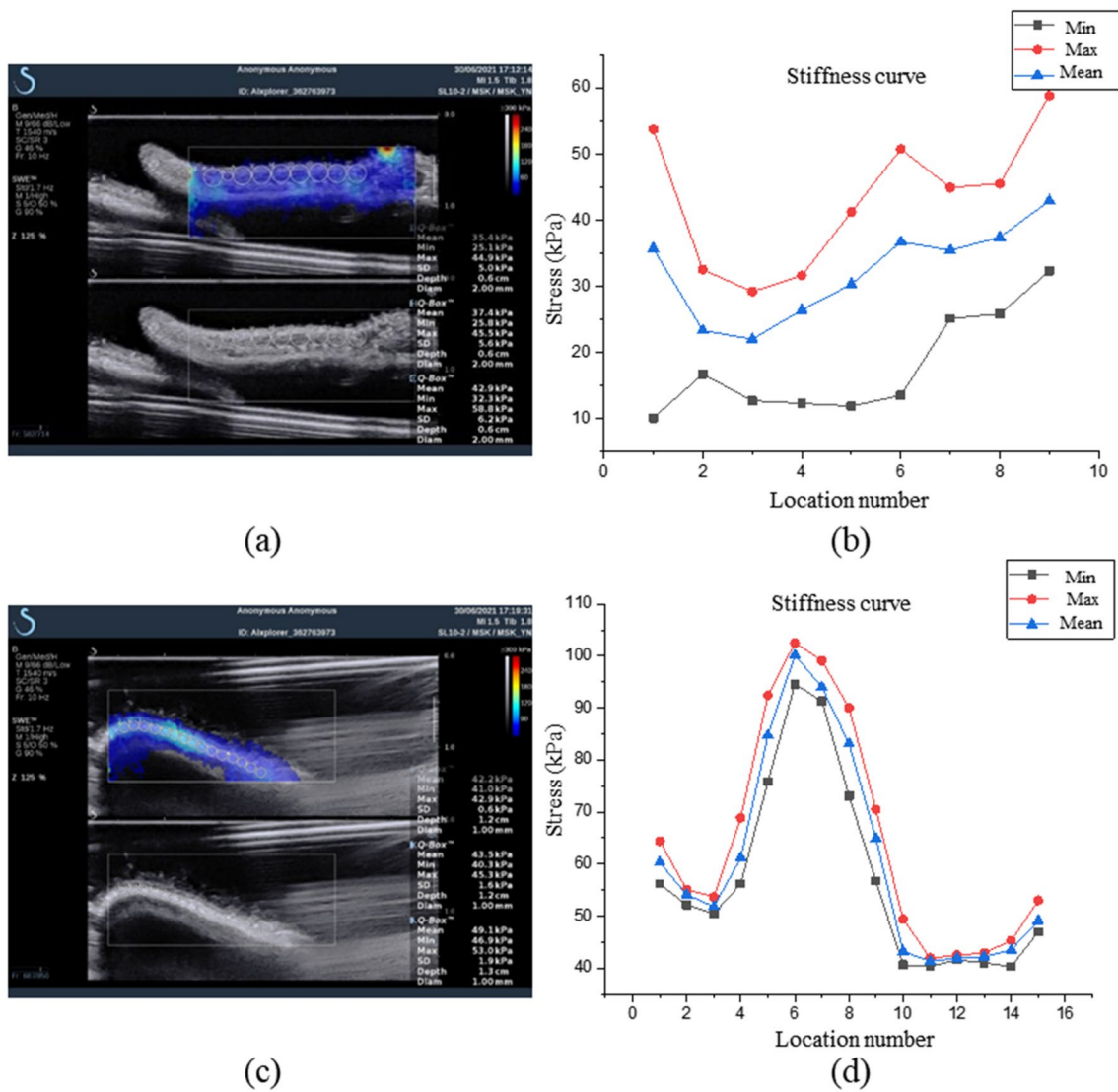
Fig. 4 The stiffness distribution of the starfish arm supported at both ends and suspended in the middle. **a** Picture of the arm when it is extended; **b** data when the arm is extended; **c** picture of the arm when it is bent; **d** data when the arm is bent

the average stress on the upper side is 19.4 kPa, and the average stress on the lower side is 40.3 kPa. The ratio of the mean value of the stress on the lower side to that on the upper side is 2.077. When the starfish arm touches the ground, the average stress on the upper side is 13.2 kPa, and the average stress on the lower side is 31.6 kPa. The ratio of the mean values of stresses on the lower side to the upper side is 2.394.

It can be found that the ratio of lower-to-upper arm stiffness is about 2. One of the reasons why the lower arm stiffness is greater than that in the upper side may be the influence of biological structure. Figure 6 shows a cross-section of the arm of a starfish, which can be divided into three regions according to the tissue structure. Area A is

the upper side of the arm. It is mainly composed of a hard bone shell with a defensive structure and relatively poor flexibility. Area B is the middle area, mainly composed of pyloric cecum (the digestive gland of starfish), ampulla and other tissues. There are also some internal cavities. Area C is the lower area of the arm, which is mainly composed of various supporting and moving bones, connective tissue between bones, muscles, and tube feet.

The mixed structure of bone, muscle, connective tissue and tube foot in area C may be the reason for greater stiffness in area C compared to area A with larger amount of shell bones. The conclusions of starfish arm stiffness gradient study also provide guidance for the structure design of biomimetic soft suction climbing robot in the following text.
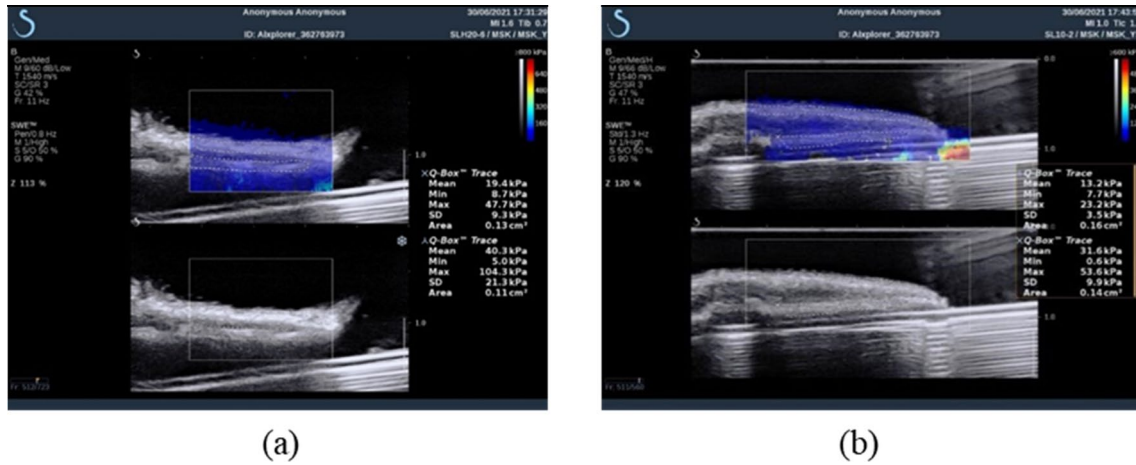
Fig. 5 Regional stiffness distribution of starfish arm. **a** Regional stiffness distribution with arm suspended; **b** regional stiffness distribution with arm attached

Table 1 Stiffness data table of starfish in different locations

	Not attached		Attached	
	Upper side (kPa)	Lower side (kPa)	Upper side (kPa)	Lower side (kPa)
Max	47.7	104.3	23.2	53.6
Min	8.7	5.0	7.7	0.6
Mean	19.4	40.3	13.2	31.6

Fig. 6 Structural stratification of the starfish arm

3 Mathematical Modeling and Material Selection of Robots

3.1 Mathematical Modeling of Tube Feet Constraints

In this article, the symmetric fiber constraint is the helical fiber constraint with two directions, as shown in Fig. 7a, the symmetric fiber constraint is obtained by mirror symmetry transformation of two asymmetric fiber constraints. The helical fibers on the surface of bionic feet are in free sliding friction contact with the surface of bionic feet, and the angles between the symmetrical helical fibers and the axis of bionic feet are denoted as β and γ.

The bionic tube feet structure is represented by solid lines under normal pressure, and the shape after inflation and pressure is represented by the dotted box. We use the differential method to analyze, and take a micro-surface unit for research. The lengths of the microfibers before and after deformation are ds and ds''. We assume that the fibers are not extensible. The Pythagorean theorem can be used on surface micro-elements. The hypotenuse is the fiber length, the leg is the axial length and the arc length in side view. The β and γ angles can be represented by two right sides of a triangle. We then have

$$ds = ds'' \tag{1}$$

$$\beta = \tan^{-1}\frac{rd\Phi}{dw}, \beta'' = \tan^{-1}\frac{r''d\Phi''}{dw''} \tag{2}$$

$$\gamma = \pi - \tan^{-1}\frac{rd\mu}{dw}, \gamma'' = \pi - \tan^{-1}\frac{r''d\mu''}{dw''} \tag{3}$$

Fig. 7 Mathematical model of the tube foot. **a** Tube foot model with symmetric fiber constraint; **b** CPG network model

(a)

(b)
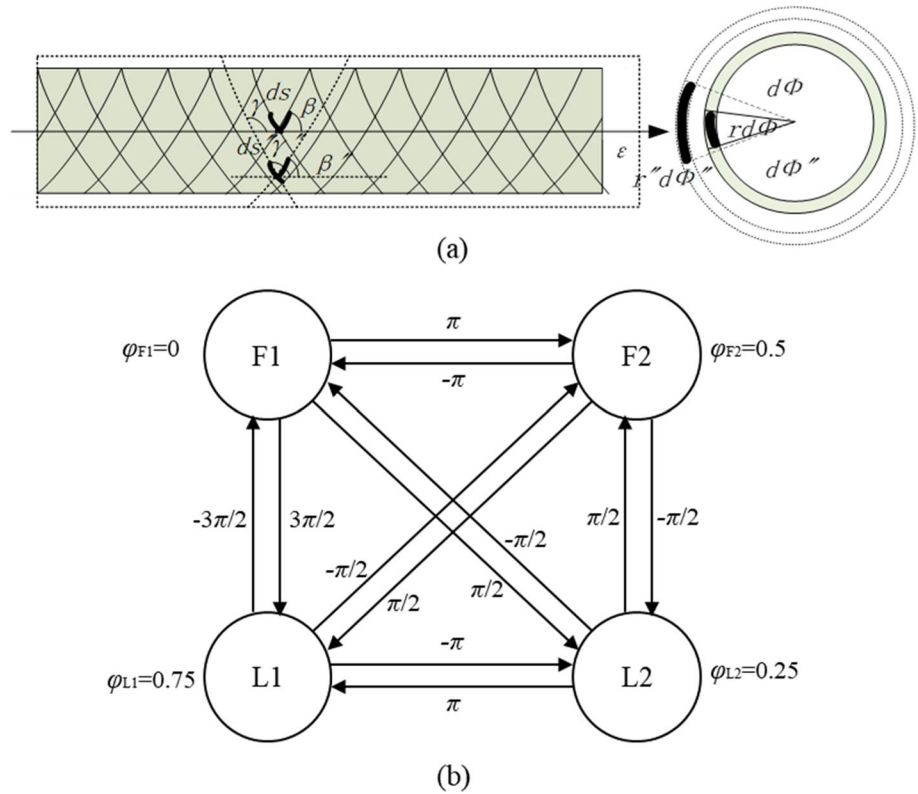
From formulas (1), (2), and (3), we can get

$$\lambda_1{}^2(\cos\beta)^2 + \lambda_2{}^2(\sin\beta)^2\left(\frac{d\Phi''}{d\Phi}\right)^2 = 1,$$

$$\lambda_1{}^2(\cos\gamma)^2 + \lambda_2{}^2(\sin\gamma)^2\left(\frac{d\Phi''}{d\Phi}\right)^2 = 1 \tag{4}$$

For uniform deformation

$$\frac{d\Phi''}{d\Phi} = \frac{\Phi''}{\Phi}, \frac{d\mu''}{d\mu} = \frac{\mu''}{\mu}, \Phi = \frac{w\tan\beta}{r}, \mu = \frac{w\tan\gamma}{r} \tag{5}$$

From the helical structure in Fig. 7a, the number of turns is related to the length w and radius r of the bionic tube foot structure, and the helical angle β can be obtained from formula (2). At the same time, it should be noted that $\Phi/2\pi$, $\mu/2\pi$ and $\Phi''/2\pi$, $\mu''/2\pi$ are the number of turns before and after the deformation of the bionic tube feet structure.

Substituting Eq. (5) into Eq. (4), the equation of the asymmetric bionic tube feet structure constraint under the premise of the final fiber inextensibility can be obtained:

$$\lambda_1{}^2(\cos\beta)^2 + \lambda_2{}^2(\sin\beta)^2\left(\frac{\Phi''}{\Phi}\right)^2 = 1,$$

$$\lambda_1{}^2(\cos\gamma)^2 + \lambda_2{}^2(\sin\gamma)^2\left(\frac{\mu''}{\mu}\right)^2 = 1 \tag{6}$$

If the fiber rotation angle before and after the surface element is inflated and pressurized is denoted as ε_i, we can get

$$\frac{d\Phi''}{d\Phi} = \frac{\Phi''}{\Phi} = \frac{\Phi + \varepsilon_i}{\Phi}, \frac{d\mu''}{d\mu} = \frac{\mu''}{\mu} = \frac{\mu + \varepsilon_i}{\mu} \tag{7}$$

From Eqs. (6) and (7), the expressions of radial stretch ratio λ_2 and rotation angle ε_i can be obtained:

$$\lambda_2 = \frac{\sqrt{1 - (\cos\gamma)^2\lambda_1{}^2}\cos\beta - \sqrt{1 - (\cos\beta)^2\lambda_1{}^2}\cos\gamma}{\sin(\beta - \gamma)}$$

$$\varepsilon_i = \frac{w}{r}\frac{\sin\beta\sqrt{1 - (\cos\gamma)^2\lambda_1{}^2} - \sin\gamma\sqrt{1 - (\cos\beta)^2\lambda_1{}^2}}{\cos\gamma\sqrt{1 - (\cos\beta)^2\lambda_1{}^2} - \cos\beta\sqrt{1 - (\cos\gamma)^2\lambda_1{}^2}} \tag{8}$$

In the above formula, w is the length of the bionic tube feet, and r is the radius of the bionic tube feet. Observing Fig. 7a, we can see that $\beta + \gamma = \pi$ in the symmetrical fiber-constrained structure. We substitute this numerical relationship into formula (8) to get

$$\varepsilon_i = 0 \tag{9}$$

Therefore, when the symmetric fiber constrains the bionic tube feet, the axis rotation angle of the bionic tube feet is zero, so the bionic tube feet structure does not rotate. The

total volume of the bionic tube feet structure after inflation and pressure deformation can be expressed as

$$V'' = \lambda_1 \lambda_2{}^2 \pi r^2 w$$

$$= \lambda_1 \left(\frac{\sqrt{1 - (\cos\gamma)^2 \lambda_1{}^2}\cos\beta - \sqrt{1 - (\cos\beta)^2 \lambda_1{}^2}\cos\gamma}{\sin(\beta - \gamma)} \right)^2 \pi r^2 \quad (10)$$

Therefore, for a bionic tube feet structure with a given lumen volume, its axial stretch ratio λ_1, radial stretch ratio λ_2 and rotation angle ε_i are all determined, and the parameters of the symmetric fiber-constrained bionic tube feet structure are unique. Therefore, the model of the bionic tube foot structure under the asymmetric unidirectional fiber constraint can be fully constrained after adding another helical fiber constraint. Two groups of constrained fibers with opposite helical directions are the simplest and most common fully constrained free fiber constraints.

3.2 Design of Control System Based on CPG Model

The main task of the CPG model is to generate stable periodic oscillating signals. To facilitate engineering applications, under the premise of ensuring that stable periodic oscillating signals can be output, a model with simple form, few parameters, small amount of calculation, easy analysis and easy realization is undoubtedly a better choice. According to this principle, this work adopts the Hopf oscillator as the unit model, which is a relatively simple harmonic oscillator, the amplitude and frequency of the output signal are easy to control, and its mathematical expression is as follows:

$$\dot{x} = \alpha(\mu - r^2)x - \omega y, \dot{y} = \alpha(\mu - r^2)y + \omega x, r^2 = x^2 + y^2 \quad (11)$$

$$\begin{bmatrix} \dot{x}_i \\ \dot{y}_i \end{bmatrix} = \begin{bmatrix} \alpha(\mu - r_i^2) & -\omega_i \\ \omega_i & \alpha(\mu - r_i^2) \end{bmatrix} \begin{bmatrix} x_i \\ y_i \end{bmatrix} + \sum_{j=1}^{4} R(\theta_i^j) \begin{bmatrix} x_i \\ y_i \end{bmatrix}, i = 1, \dots, 4 \quad (12)$$

$$\omega_i = \frac{\omega_{st}}{e^{-\alpha y_i} + 1} + \frac{\omega_{sw}}{e^{\alpha y_i} + 1}, \omega_{st} = \frac{1 - \beta}{\beta} \omega_{sw} \quad (13)$$

In the formula, ω_{sw} and ω_{st} are the rising frequency and falling frequency of the output signal, respectively. The parameter α determines the speed at which ω changes between ω_{sw} and ω_{st}. α is a positive constant and β is the load factor. x_i is the output of the oscillator, as the bending control signal. y_i is the adsorption control signal. The second term on the right is the inter-oscillator coupling term. θ_i^j is the relative phase with the oscillator. $R(\theta_i^j)$ is the rotation matrix, which describes the phase coupling relationship between the oscillators:

$$R(\theta_i^j) = \begin{bmatrix} \cos\theta_{ji} & -\sin\theta_{ji} \\ \sin\theta_{ji} & \cos\theta_{ji} \end{bmatrix} \quad (14)$$

Both the bending control signal and the adsorption control signal are binarized to correspond to the bending and adsorption states of the foot structure. Changing α, μ, ω, and β can change the dynamic performance of the oscillator, corresponding to the convergence speed, amplitude, period and shape of the signal, respectively. We established a CPG network model, a total of 4 oscillators, the oscillator LF is the reference oscillator, the rest of the oscillators corresponds to the number of the control foot unit, and the coupling relationship between the oscillators is shown in Fig. 7b.

3.3 Constitutive Model and Material Test

Polynomial model, reduced polynomial model and Ogden model are used for fitting in Abaqus software, the red curve in the Fig. 8a is the raw data of Ecoflex-0030 tensile test. In the small deformation stage, all the models can fit the original data well, but in the large deformation stage, only Yeoh model, Arruda-Boyce model and reduced polynomial model (when $N = 4$) are more suitable for the original stress–strain data of Ecoflex-0030 silicone rubber material, while Ogden model, polynomial model (when $N = 1, 2$) and the reduced polynomial model (when $N = 1, 5$) produced larger errors. Considering a variety of factors for re-fitting, the Yeoh model was finally selected as the constitutive model that is the R_POLY_N3 curve in Fig. 8b of the Ecoflex-0030 silicone rubber material. The parameters of the model are shown in Table 2.

4 Structural Design and Manufacturing

4.1 Structural Design

We studied the structure of starfish tube feet and end suction cups and body structure, and designed the structure of the bionic starfish soft body robot accordingly. According to Fig. 2, we obtained the overall structure of the starfish arm and the surface structure of the tube foot. The surface layer of the tube foot is composed of intersecting fibrous muscle tissue. Based on this, we conducted mathematical modeling of the robot's legs. In addition, the surface of the robot's legs has cross-fiber constraints to realize the elongation and bending functions of the leg. At the same time, Fig. 2 also reveals that the water vascular system of starfish has a valve flap structure, which can prevent backflow of body fluids and can also shield some injured feet. Based on this, we realized the function of cutting off the energy supply of some broken legs individually in the

Fig. 8 Fitted model data of Eco-flex-0030 compared with real data. **a** First fit data; **b** second fit data
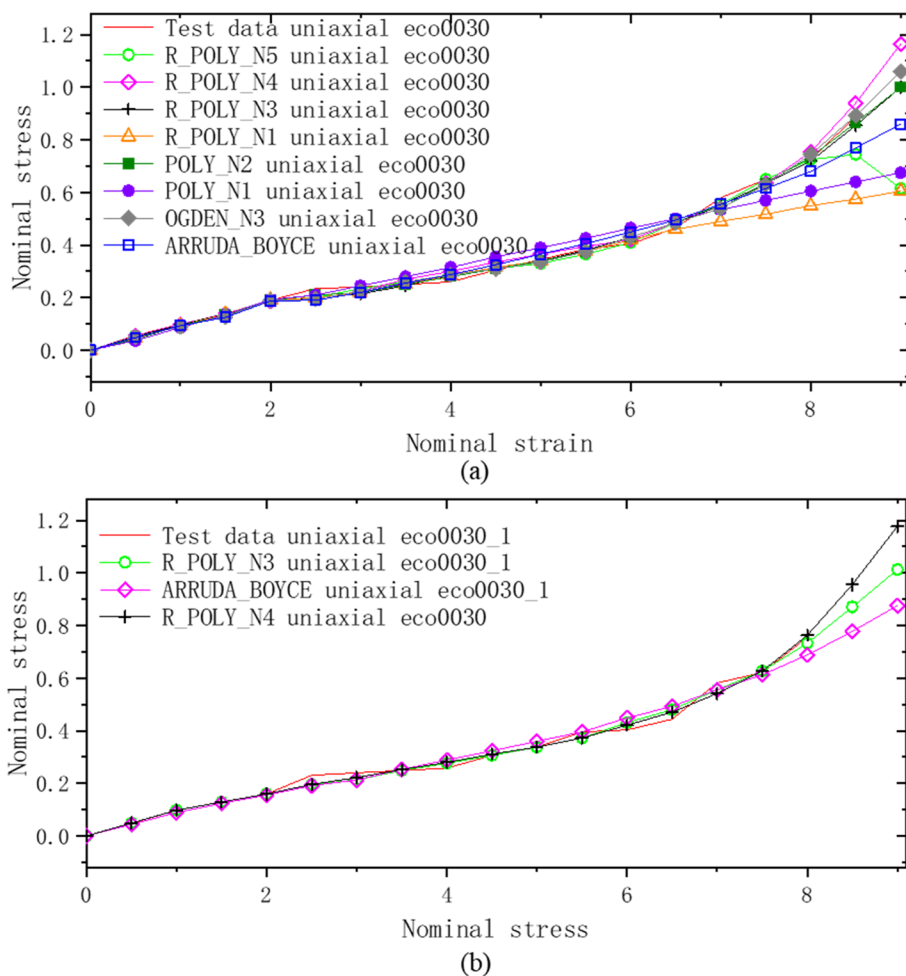

Table 2 Yeoh model parameters

Value	C10	C20	C30	D1	D2	D3
Value	2.9E−2	− 6.4182E−5	1.1862E−6	2.1185	0	0

control. According to Figs. 3, 4 and 5, we can find that the stiffness ratio of the lower and upper parts of the starfish body is about 2. Therefore, the stiffness ratio between the lower side and the upper side of the robot body is also designed to be 2. The legs and feet of the soft robot correspond to the tube feet of the starfish, and the body of the soft robot corresponds to the starfish arm structure (Fig. 9). The overall structure of the robot can be divided into multiple layered structures. The overall structure of the robot is composed of the upper working layer, the middle active adaptation layer, the lower connecting layer, the variable stiffness layer and the bionic feet layer.

The main structure of the bionic starfish soft robot is shown in Fig. 10. The material used in the main structure of the bionic tube feet is Ecoflex-0030 silicone material. The fixed ring is made of resin 3D printing, and there are several small holes on the ring to fix the fibers. The high-strength fibers are evenly wound on the surface of the tube feet structure at an angle of θ to the axis of the cylinder, which is used to limit the radial expansion of the tube feet structure and improve the load capacity of the lumen to pressure, and improve the overall stiffness of the feet structure. The bottom suction cup is also made of Ecoflex-0030 silicone material, and the suction cup mainly realizes the adsorption function.

To make the bionic suction and climbing software robot adapt to the complex curved surface of narrow space with variable curvature, two active adaptive layer structures are designed according to the principle that the starfish arm can bend actively, both of these two structures achieve bending due to the asymmetry of the structure and the difference in the expansion range of the high-pressure gas. The active adaptation layer structure can be divided into two types: the vertical structure is 120 mm long and
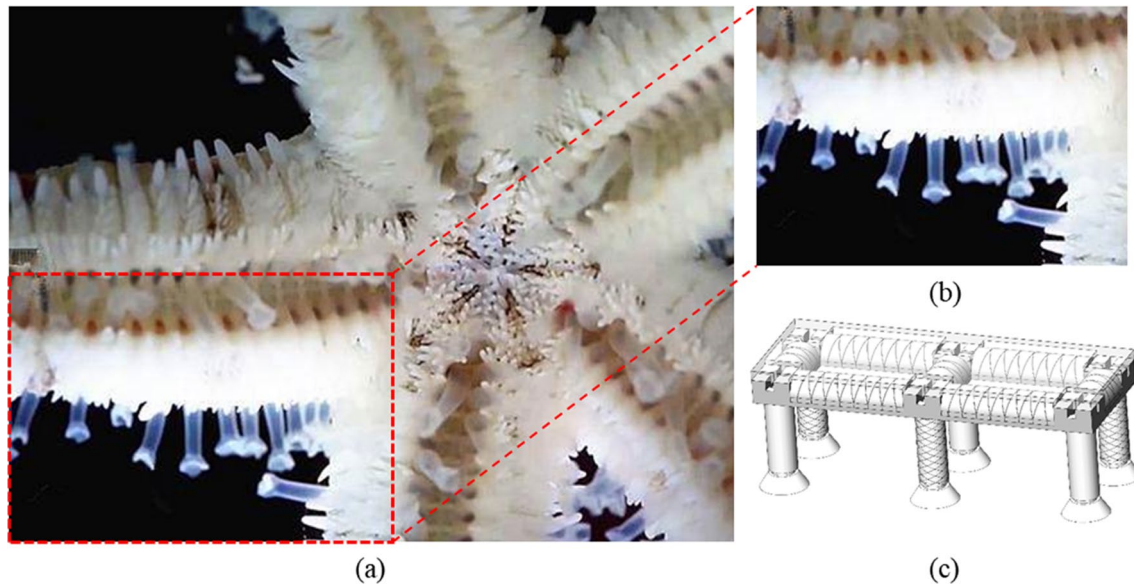
Fig. 9 Comparison between starfish and soft robots. **a** Front view of a starfish; **b** enlarged view of tube foot; **c** bionic soft robot

40 mm wide, the horizontal structure is 50 mm long and 40 mm wide. The radius of the internal semicircular chamber is 15 mm and the wall thickness is 5 mm. To ensure the uniform winding of the fibers, we have designed grooves on the outer surface of the active adaptation layer structure according to the designed path, and the depth of the grooves is 0.5 mm. If there is no helical groove, the outer surface of the active adaptation layer structure is relatively smooth, so the fibers will slip after multiple bending movements, and lose the proper restraint effect and destroy the symmetry of the active adaptation layer structure. Variable stiffness layers achieve stiffness changes by the principle of line blocking.

4.2 Manufacturing Process

The production process of the bionic tube foot structure consists of six steps: assembling the mold, making and defoaming with silica gel, pouring and stewing, mold opening, overall installation, and fiber fixing (Fig. 11a).

After the upper and lower platform structures, the symmetric and asymmetric bionic tube foot structures, the longitudinal and transverse structures of the active adaptation layer, and the variable stiffness layer structure are fabricated, the overall installation is carried out. The installation steps are as follows: (1) installation of the bionic tube foot, (2) installation of the active adaptation layer, (3) further sealing and fixing, (4) installation of the upper bearing layer platform, and (5) installation of the variable stiffness layer (Fig. 11b).

5 Experiment and Analysis

5.1 Hardware System Construction

The control system can be divided into electrical part and pneumatic part. The electrical part includes controllers, pressure sensors, relays, and power supplies. The pneumatic part consists of a solenoid valve, a pressure reducing valve, a vacuum pump, an air compressor, and a pneumatic execution structure on a software robot (Fig. 12).

The controller realizes the purpose of controlling the strong electricity by weak electricity through the relay. The relay controls the direction of the solenoid valve to realize whether the air source is connected or not. The negative pressure provided by the vacuum pump is also switched on and off by the same principle. The function of the pressure reducing valve is to achieve the function of voltage stabilization and protection, because the gas in the air compressor is in a state of higher pressure. If the pressure relief valve is not installed, the pneumatic actuator structure of the soft robot cannot withstand too much air pressure, and structural damage will occur. In terms of negative pressure, a pressure reducing valve is not required. Since it is limited by the power and mechanical structure of the vacuum pump, too much vacuum cannot be generated, so the protection device is not needed. The controller uses the pressure signal returned by the pressure sensor to monitor the state of the software robot according to the designed algorithm.
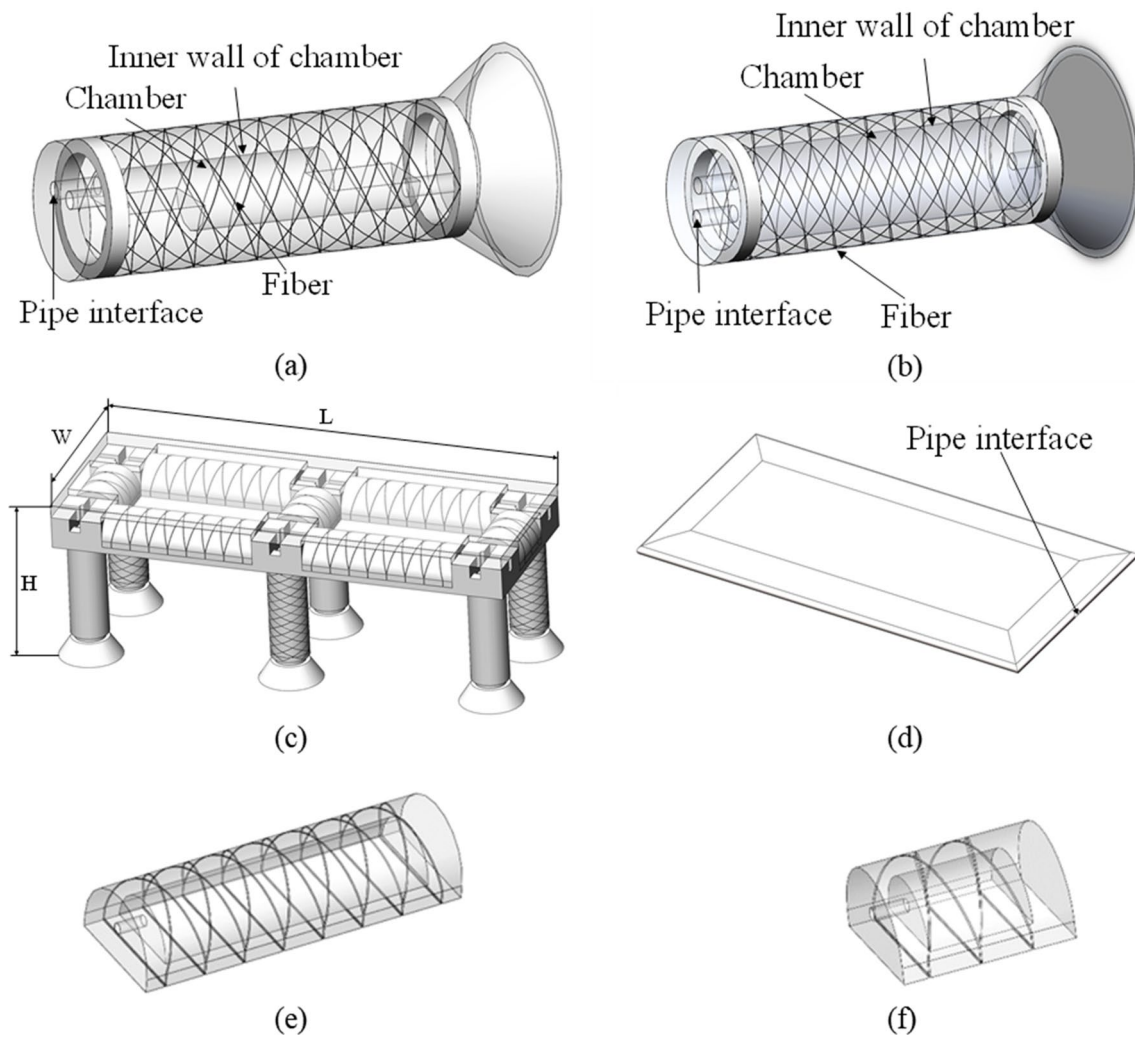
Fig. 10 The structure of each part of the bionic soft robot. **a** Bionic tube foot with bending and elongation function; **b** bionic tube foot with bending function only; **c** overall model of the soft robot; **d** vari- able stiffness structure; **e** longitudinal structure of the active adaptation layer; **f** transverse structure of the active adaptation layer

5.2 Tube Foot Test

First, an elongation experiment was performed on a single symmetrical bionic tube foot (Fig. 13a), and the data are shown in Fig. 13c. It can be seen from the figure that as the air pressure increases, its length also increases, and the rate of length increase increases. When the pressure value increased to 0.03 MPa, the deformation degree of the symmetrical bionic tube foot reached the maximum, and the maximum elongation was about 32.65%.

After that, the response speed of the bionic tube foot deformation was tested. Since the air pressure value is greater than 0.03 MPa, the structure is too elongated and not suitable for walking, so the given air pressure value is set to 0.03 MPa. The relationship between the elongation length of the bionic tube foot and the time to reach the steady state was recorded to test the response speed of the structure.

The test results are shown in Fig. 13d, and the steady state is reached at about 250 ms.

Step elongation experiments were performed on a single asymmetric bionic tube foot (Fig. 13b), and the data are shown in Fig. 13e and f. It can be seen from the figure that there is a positive correlation between air pressure and elongation. The elongation increases approximately linearly between 0.015 and 0.03 MPa, and the change in air pressure causes a smaller degree of change in elongation when the air pressure is small. When the pressure value increases to 0.03 MPa, the elongation of the asymmetric bionic foot is already large enough. At this point, if you continue to increase the value of the pressure, its elongation is no longer suitable for walking. The maximum elongation is about 36.73% and the step distance is 8.18 mm.

Figure 14a shows the method of adsorption experiments. The suction cup at the end of the bionic tube foot
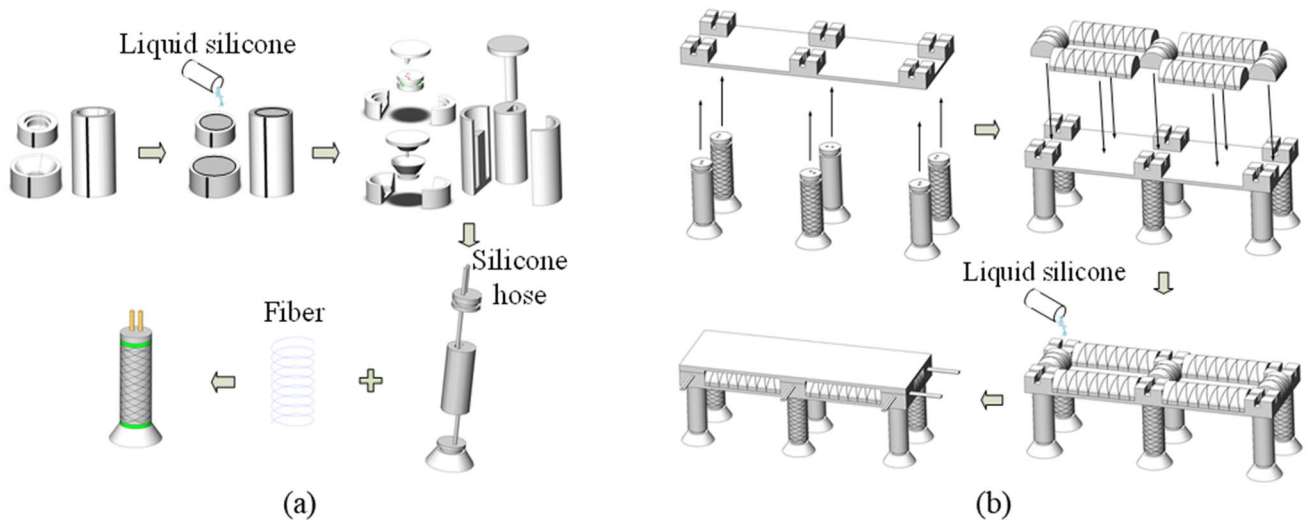
Fig. 11 Fabrication process of key components. **a** Fabrication steps of bionic tube foot; **b** overall installation process
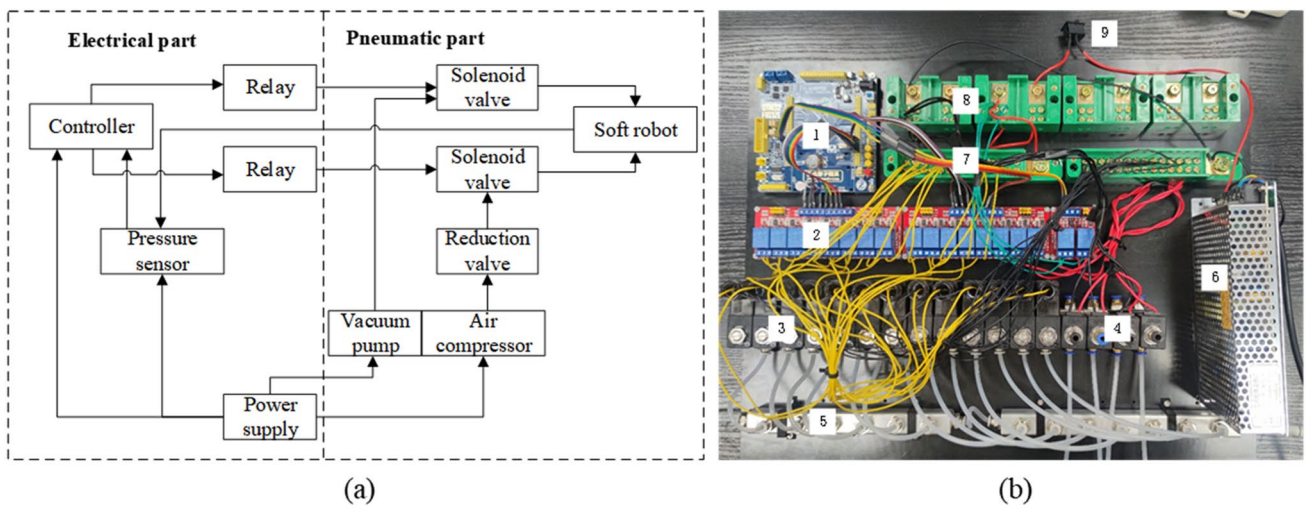

Fig. 12 Control system structure. **a** Relationship between multiple modules; **b** the construction of the control system of the soft robot

is adsorbed on the material to be tested, and a weight platform is connected under the material to be tested. Gradually increase the weight on the weight platform until the suction cup is separated from the adsorption matrix, record the weight of the weight at this time, and perform multiple repeated tests to obtain the average value. Plot the surface relationship between the suction force and the negative pressure provided. Observing Fig. 14b, it can be found that the relationship between the adsorption force of the bionic tube foot suction cup and the vacuum degree is very similar on the metal and glass surfaces. For the wood surface, the adsorption force is smaller than the other two under the same vacuum degree. The reason is that the wood surface is rough and there is gas leakage in the vacuum area inside the

suction cup. To ensure the safety of the overall adsorption, as shown in Fig. 14c, a self-detection function for surface fitting is designed in this paper. If the foot end is in contact with the curved surface, pressure is applied to the embedded pressure sensor, otherwise there is no pressure. In this way, the supply pressure can be cut off in the area where the robot fails to ensure safety.

5.3 Bending Test and Variable Stiffness Test

Bending test experiments are carried out on the longitudinal and transverse structures of the active adaptive layer. As can be seen in Fig. 15c and d, there is a positive correlation between air pressure and elongation. The slope of the
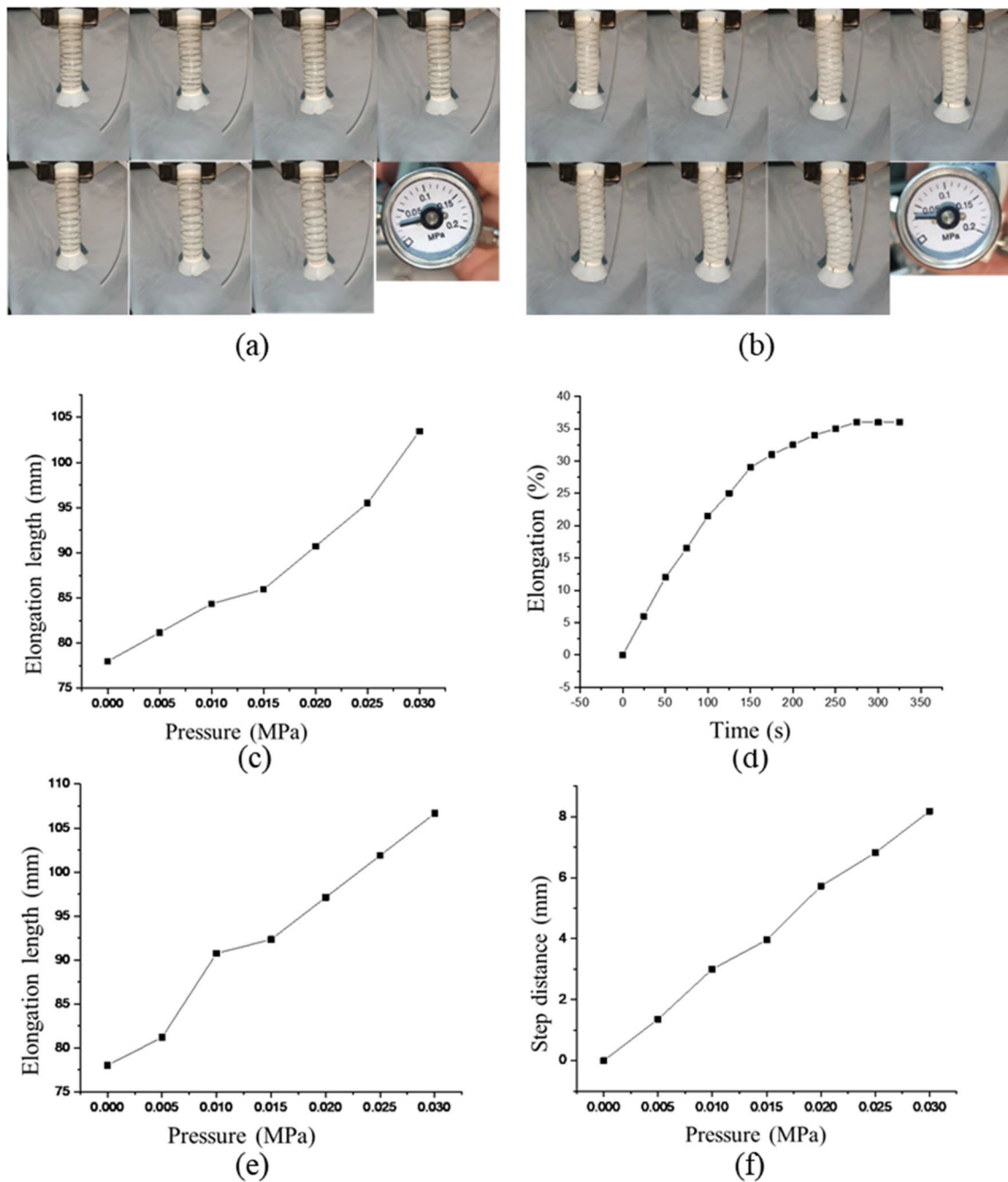
(a)

(b)

(c)

(d)

(e)

(f)

Fig. 13 Pressure tests on two bionic tube feet. **a** Experiment on tube feet with elongation function, **b** experiment on a tube foot with bending and elongation functions, **c** relationship between elongation length and pressure of an elongated tube foot, **d** response time of elongated foot, **e** relationship between elongation length and pressure for bent elongated foot, and **f** relationship between step distance and pressure for bending elongated tube feet

elongation increases between 0.005 and 0.03 MPa. When the air pressure is small, the change of the air pressure causes a small change in the bending angle. When the pressure value increases to 0.03 MPa, the bending angle of the longitudinal structure is large enough. At this time, continue to increase the value of the pressure, and the bending angle has exceeded 180°, which is not suitable for surface adaptation.

The maximum bending angle of the longitudinal structure is 183.2°, and the maximum bending angle of the transverse structure is 36.4°. It should also be noted that confinement failure can occur when overpressure is applied to shorter structures.

A load is applied to one edge of the variable stiffness layer with a dynamometer, and the load gradually changes

Fig. 14 Adsorption experiment and contact detection. **a** Adsorption experiment design; **b** relationship between different surface adsorption force and vacuum pressure; **c** surface fit self-detection
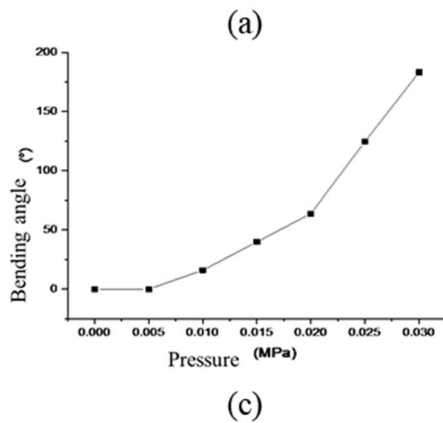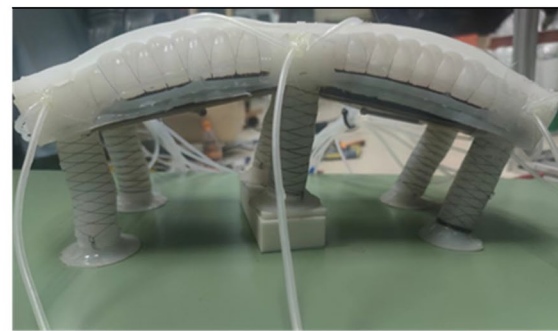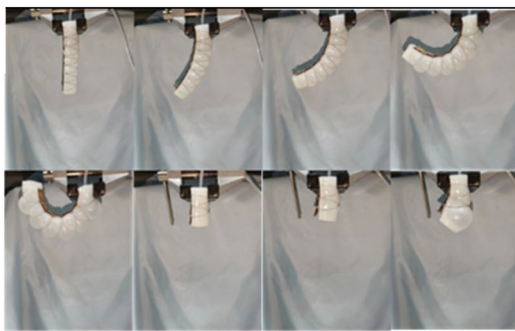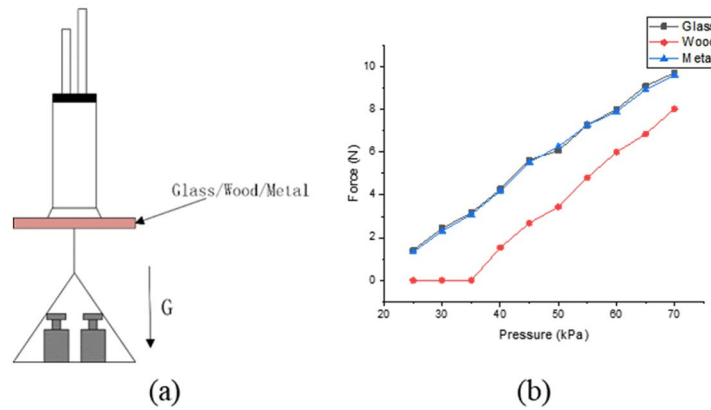

(a)

(b)

(c)

(a)

(b)

(c)

(d)
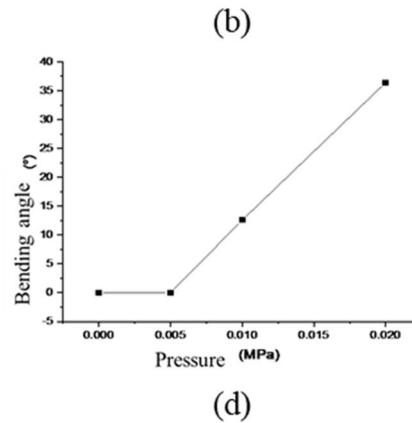
Fig. 15 Bending experiments of active adaptive layers. **a** Bending process of two structures; **b** soft robot can change the degree of body bending; **c** relationship between bending angle and pressure in longi-tudinal structure; **d** relationship between bending angle and pressure of transverse structure

from small to large. Record the deflection changes of the variable stiffness layer with and without negative pressure, and draw a graph of the relationship between load force and displacement under these two conditions, as shown in Fig. 16d.

It can be found that when no negative pressure is provided, the load force and displacement are basically linear. Stiffness does not change substantially. When negative pressure is provided, when the load force is small,

the curve is basically linear, and the stiffness is basically unchanged. With the increase of the load force, when the displacement reaches about 17 mm, the slope of the curve begins to decrease, which means that the stiffness of the variable stiffness layer is decreasing. When the displacement reaches about 28 mm, the slope of the curve is basically unchanged, and the stiffness is also stabilized at this time. It can be found that with negative pressure even when the stiffness is minimal, the stiffness is greater than
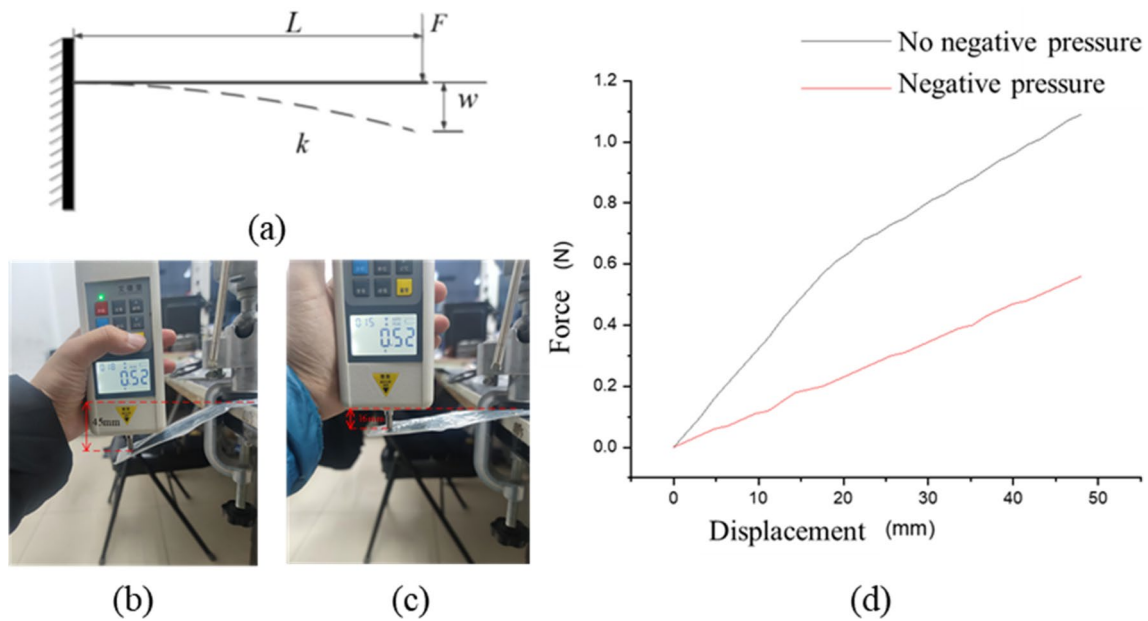
Fig. 16 Stiffness experiments of the variable stiffness structure. **a** Principle of stiffness experiment; **b** variable stiffness structures do not work; **c** variable stiffness structures work; **d** the relationship between force and displacement of the variable stiffness structure
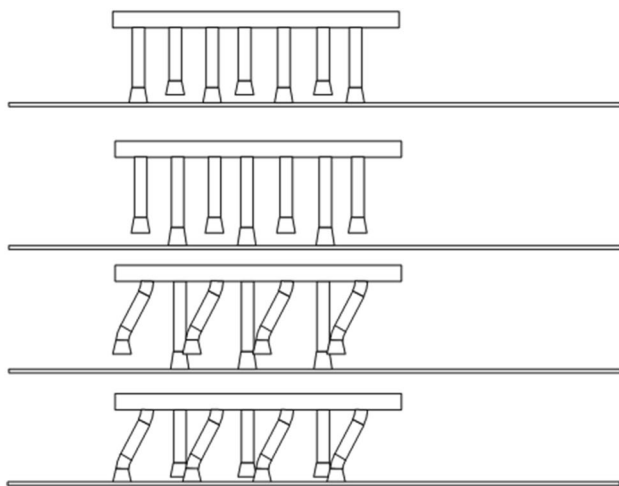

Fig. 17 Walking logic diagram of soft robot

that without negative pressure. The ratio of the maximum stiffness with negative pressure to the stiffness without negative pressure is 2.8125.

5.4 Motion Test

The logic diagram of the robot walking is shown in Fig. 17. The robot's symmetrical tube feet are first attached to the substrate and then elongated. The asymmetrical feet are

separated from the base body, and then the asymmetrical feet are bent and stepped and suspended. Symmetrical tube feet close ventilation and platform height is lowered. At this time, the end suction cup of the asymmetrical feet is in contact with the substrate and adsorbed, and then the suction cup of the symmetrical feet is desorbed. The asymmetrical feet are restored to their initial state, and the next cycle of walking is performed.

The actual robot is shown in Fig. 18a. The overall robot was tested for plane walking and surface walking. The experimental data are shown in Fig. 18d and e. The walking speed of the robot on the plane is about 1.51 mm/s, and the walking speed on the curved surface is about 1.56 mm/s. Factors affecting the speed of movement include control oscillation signal period, gas flow rate and so on.

6 Conclusions

Inspired by the structure and motion of starfish, a new bionic starfish soft wall-climbing robot was developed by studying the biological structure of starfish to adapt to the special working environment of narrow space, complex surface and non-magnetic medium such as the internal surface of aircraft. The robot consists of five parts: upper working layer, central active adaptation layer, lower connection layer, variable stiffness layer, and bionic foot layer. The novel design of the active adaptation layer allows the soft robot to adapt to complex curved surfaces. The bionic tube foot is designed to adapt to a variety of magnetic or

Fig. 18 Soft robot walking experiment. **a** Physical object of soft robot; **b** walking on flat surface; **c** walking on curved surfaces; **d** flat surface walking data; **e** curved surface walking data
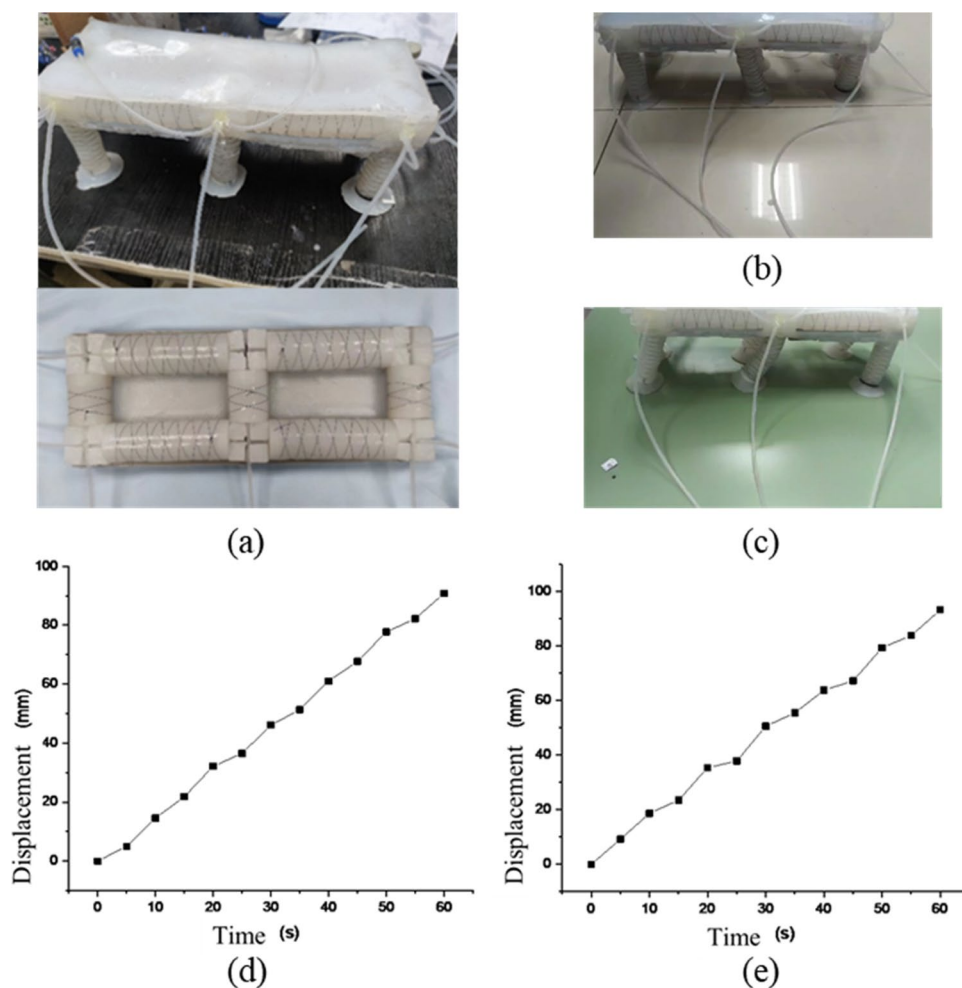
non-magnetic surfaces. The control model of the soft robot is also proposed, the central pattern generator theory is introduced, and the walking gait is designed. Based on this, the relationship between the bionic tube foot and pressure, as well as the robot walking speed on planes and surfaces are obtained through prototype tests. The research results show that high surface adaptability of the flexible crawling robot can be achieved using a novel design and a suitable control method.

Declarations

Conflict of Interest The author (Yanqiang Liu) declares that there is no competing interest.

References

1. Niu, H. Q., Feng, R. Y., Xie, Y. W., Jiang, B. W., Sheng, Y. Z., Yu, Y., Baoyin, H. X., & Zeng, X. Y. (2021). Magworm: A bio-mimetic magnet embedded worm-like soft robot. *Soft Robotics, 8*(5), 507–518. https://doi.org/10.1089/soro.2019.0167
2. Bell, M. A., Pestovski, I., Scott, W., Kumar, K., Jawed, M. K., Paley, D. A., Majidi, C., Weaver, J. C., & Wood, R. J. (2018).

Echinoderm-inspired tube feet for robust robot locomotion and adhesion. *IEEE Robotics and Automation Letters, 3*(3), 2222–2228. https://doi.org/10.1109/LRA.2018.2810949

3. Yuan, P. Z., & Tsukagoshi, H. (2021). Double helical soft pneumatic actuator capable of generating complex 3D torsional motions. *IEEE Robotics and Automation Letters, 6*(4), 8142–8149. https://doi.org/10.1109/LRA.2021.3102940

4. Jumet, B., Bell, M. D., Sanchez, V., & Preston, D. J. (2022). A data-driven review of soft robotics. *Advanced Intelligent Systems, 4*(4), 2100163. https://doi.org/10.1002/aisy.202100163

5. Zhou, D., Fu, Y., Deng, J., Sun, J., & Liu, Y. X. (2021). A bistable jumping robot with pure soft body actuated by twisted artificial muscle. In: *2021 27th International conference on mechatronics and machine vision in practice (M2VIP)*, Shanghai, China (pp. 388–393). https://doi.org/10.1109/M2VIP49856.2021.9665013

6. Chang, A. H., Freeman, C., Mahendran, A. N., Vikas, V., & Vela, P. A. (2021). Shape-centric modeling for soft robot inchworm locomotion. In: *2021 IEEE/RSJ international conference on intelligent robots and systems (IROS), electr network* (pp. 645–652). https://doi.org/10.1109/IROS51168.2021.9636695

7. Krishnan, G., Bishop-Moser, J., Kim, C., & Kota, S. (2012). Evaluating mobility behavior of fluid filled fiber-reinforced elastomeric enclosures. In: *ASME international design engineering technical conferences and computers and information in engineering conference*, Chicago, IL, USA (Vol. 45035, pp. 1089–1099). https://doi.org/10.1115/detc2012-71278

8. Wang, T., Zhang, J. H., Zhao, G., Li, Y., Hong, J., & Wang, M. Y. (2018),An inchworm-inspired rigid-reinforced soft robot with combined functions of locomotion and manipulation. In: *2018 IEEE/ASME international conference on advanced intelligent mechatronics (AIM)*, Auckland, New Zealand (pp. 1087–1091). https://doi.org/10.1109/aim.2018.8452680

9. Shintake, J., Rosset, S., Schubert, B., Floreano, D., & Shea, H. (2016). Versatile soft grippers with intrinsic electroadhesion based on multifunctional polymer actuators. *Advanced Materials, 28*(2), 231–238. https://doi.org/10.1002/adma.201504264

10. Pi, J., Liu, J., Zhou, K. H., & Qian, M. Y. (2021). An octopus-inspired bionic flexible gripper for apple grasping. *Agriculture, 11*(10), 1014. https://doi.org/10.3390/agriculture11101014

11. Manti, M., Hassan, T., Passetti, G., D'Elia, N., Laschi, C., & Cianchetti, M. (2015). A bioinspired soft robotic gripper for adaptable and effective grasping. *Soft Robotics, 2*(3), 107–116. https://doi.org/10.1089/soro.2015.0009

12. Gong, Z. Y., Fang, X., Chen, X. Y., Cheng, J. H., Xie, Z. X., Liu, J. Q., Chen, B. H., Yang, H., Kong, S. H., Hao, Y. F., Wang, T. M., Yu, J. Z., & Wen, L. (2021). A soft manipulator for efficient delicate grasping in shallow water: Modeling, control, and real-world experiments. *The International Journal of Robotics Research, 40*(1), 449–469. https://doi.org/10.1177/0278364920917203

13. Wang, Y. X., & Xu, Q. S. (2019). Design and fabrication of a new dual-arm soft robotic manipulator. *Actuators, 8*(1), 5. https://doi.org/10.3390/act8010005

14. Liu, Z. S., Zhang, R., Xiao, Y. C., Li, J. T., Chang, W., Qian, D., & Liu, Z. F. (2021). Somatosensitive film soft crawling robots driven by artificial muscle for load carrying and multi-terrain locomotion. *Materials Horizons, 8*(6), 1783–1794. https://doi.org/10.1039/d1mh00457c

15. Bartlett, N. W., Tolley, M. T., Overvelde, J. T. B., Weaver, J. C., Mosadegh, B., Bertoldi, K., Whitesides, G. M., & Wood, R. J. (2015). A 3D-printed, functionally graded soft robot powered by combustion. *Science, 349*(6244), 161–165. https://doi.org/10.1126/science.aab0129

16. Liao, B., Zang, H. B., Chen, M. Y., Wang, Y. J., Lang, X., Zhu, N. N., Yang, Z., & Yi, Y. (2020). Soft rod-climbing robot inspired by winding locomotion of snake. *Soft Robotics, 7*(4), 500–511. https://doi.org/10.1089/soro.2019.0070

17. Chen, X. T., Stegagno, P., & Yuan, C. Z. (2021). A cable-driven switching-legged inchworm soft robot: design and testing. In: *2021 American control conference (ACC), electr network* (pp. 2–7). https://doi.org/10.23919/acc50511.2021.9482921

18. Kandhari, A., Mehringer, A., Chiel, H. J., Quinn, R. D., & Daltorio, K. A. (2019). Design and actuation of a fabric-based worm-like robot. *Biomimetics, 4*(1), 13. https://doi.org/10.3390/biomimetics4010013

19. Zheng, Z. Y., Zhao, Y. R., & Wang, G. (2023). Research on piezoelectric driving microminiature three-legged crawling robot. *Journal of Bionic Engineering*. https://doi.org/10.1007/s42235-023-00350-0

20. Su, M. J., Xie, R. Z., Qiu, Y., & Guan, Y. S. (2023). Design, mobility analysis and gait planning of a leech-like soft crawling robot with stretching and bending deformation. *Journal of Bionic Engineering, 20*(1), 69–80. https://doi.org/10.1007/s42235-022-00256-3

21. Jin, H., Dong, E. B., Alici, G., Mao, S. X., Min, X., Liu, C. S., Low, K. H., & Yang, J. (2016). A starfish robot based on soft and smart modular structure (SMS) actuated by SMA wires. *Bioinspiration & Biomimetics, 11*(5), 056012. https://doi.org/10.1088/1748-3190/11/5/056012

22. Yang, X., Tan, R., Lu, H. J., & Shen, Y. J. (2021). Starfish inspired milli soft robot with omnidirectional adaptive locomotion ability. *IEEE Robotics and Automation Letters, 6*(2), 3325–3332. https://doi.org/10.1109/LRA.2021.3062823

23. Poungrat, A., & Maneewarn, T. (2017). A starfish inspired robot with multi-directional tube feet locomotion. In: *2017 IEEE international conference on robotics and biomimetics (ROBIO)*, Macau, China (pp. 712–717). https://doi.org/10.1109/robio.2017.8324501

24. Munadi, M., Ariyanto, M., Setiawan, J. D., & Al Ayubi, M. F. (2018). Development of a low-cost quadrupedal starfish soft robot. In: *2018 5th international conference on information technology, computer, and electrical engineering (ICITACEE)*, Semarang, Indonesia (pp. 225–229). https://doi.org/10.1109/icitacee.2018.8576931